

A semiparametric spatio-temporal model for solar irradiance data

Joshua D. Patrick

*Department of Statistics, One Shields Avenue, University of California, Davis, CA
95616-5270*

Jane L. Harvill

*Department of Statistical Science, P.O. Box 97140, Baylor University, Waco, TX
76798-7140*

Clifford W. Hansen

P.O. Box 5800, Sandia National Laboratories, Albuquerque, NM 87185-1033

Abstract

Design and operation of a utility scale photovoltaic (PV) power plant depends on accurate modeling of the power generated, which is highly correlated with aggregate solar irradiance on the plant's PV modules. At present, aggregate solar irradiance over the area of a typical PV power plant cannot be measured directly. Rather, irradiance measurements are typically available from a few, relatively small sensors and thus aggregate solar irradiance must be estimated from these data. As a step towards finding more accurate methods for estimating aggregate irradiance from available measurements, we evaluate semiparametric spatio-temporal models for global horizontal irradiance. Using data from a 1.2 MW PV plant located in Lanai, Hawaii, we show that a semiparametric model can be more accurate than simple interpolation between sensor locations. We investigate spatio-temporal models with separable and nonseparable covariance structures and find no evidence to support assuming a separable covariance structure.

Keywords: Irradiance, Models, Spatio-temporal model, Nonseparability, Lattice data, Semiparametric time series

1. Introduction

Accurate modeling of power output from utility scale photovoltaic (PV) power plants is often key to obtaining favorable financial terms during system design and construction, and to efficient and profitable plant operation. Accurate modeling of power output requires estimating aggregate plane-of-array (POA) irradiance over the plant’s footprint with sufficient precision, because aggregate POA irradiance is highly correlated with power output (Kuszamaul et al., 2010).

There is great interest in methods to improve the accuracy of estimates of aggregate irradiance used for PV power plant modeling. Error in estimating the aggregate irradiance translates directly to error in modeled power output and thus to error in projected energy production; relatively small errors in projected energy may translate to significant uncertainty in projected profit because utility-scale PV plants are typically leveraged financially.

Here, we explore statistical modeling of global horizontal irradiance (GHI) at spatial and temporal scales relevant to design and operation of a utility-scale PV power plant, i.e., on the order of 1 km^2 and a few minutes. We apply recent advances in spatio-temporal statistical methods and illustrate our results with data from a 1.2MW PV plant at La Ola, Lanai, HI. We pursue semiparametric (i.e., data-driven) rather than parametric approaches because a successful model could then be applied regardless of weather conditions at the location of interest. In contrast, parametric models implicitly assume that random variables in the model (e.g., GHI) are well-described by specified distributions, an assumption which may not hold if weather conditions change. We compare the resulting models with the commonly used simple spatial average which estimates aggregate irradiance over a plant’s footprint by averaging measurements from sensors located in or near the plant.

A challenge in modeling irradiance data is incorporating the interaction between time and space. Especially in the presence of advecting clouds, the irradiance observed at one location is likely to also be observed at other locations but with a time shift. Thus we anticipate that irradiance will exhibit a spatial autocorrelation that varies with time. Spatio-temporal models explicitly account for this autocorrelation and thus may predict aggregate irradiance more accurately than does a simple spatial average.

Fundamentally, GHI can be viewed as a random spatio-temporal process. Literature reports several efforts at modeling individual time-series of irradi-

ance, and substantially fewer attempts to construct spatio-temporal models of irradiance considering several proximal locations. The literature on individual time-series modeling includes approaches based on autoregressive integrated moving average (ARIMA) analysis (e.g., Yang et al., 2012), non-linear autoregressive analysis (Glasbey, 2001), regression analysis (Reikard, 2009), artificial neural networks analysis (Paoli et al., 2010), k -Nearest Neighbors algorithm (Paoli et al., 2010) and Bayesian inference (Paoli et al., 2010). These approaches focus on forecasting irradiance considering only the measurements at a selected location separately from measurements at other locations. Paoli et al. (2010) considers a type of artificial neural network known as Multi-Layer Perceptron (MLP) network and finds their method performs as well or better than other methods such as ARIMA analysis, Bayesian inference, and k -Nearest Neighbors. Yang et al. (2012) introduce an ARIMA model that incorporates low-resolution, ground-based cloud cover data to obtain next hour solar irradiance. The authors state that their ARIMA model outperforms all other time series forecasting methods in four of the six stations they tested. In both the MLP and ARIMA methods, the model does not incorporate a spatial component but only models irradiance in time.

The literature on spatio-temporal modeling of solar irradiance is limited. To our knowledge, ours is the first attempt to model irradiance at time and spatial scales relevant to modeling a utility-scale PV plant. Glasbey and Allcroft (2008) model irradiance data from ten sensors roughly at 5km spacing using a spatio-temporal autoregressive moving average (STARMA) model. The STARMA model incorporates the Euclidian distances between two points in order to model the spatial structure of the data. However, the STARMA model used in Glasbey and Allcroft (2008) assumes a separable covariance structure, an assumption which we find to be questionable at the scale of a single PV plant.

We propose a spatio-temporal model that incorporates a data-driven method for modeling the time series component. Our model improves upon the works of Yang et al. (2012) and Glasbey (2001) because we do not assume a parametric form for the time component of the model, and improves on Glasbey and Allcroft (2008) through the nonseparable covariance structure. The remainder of this paper is organized as follows. In Section 2, we discuss how the time series structure is modeled via a semiparametric model fitted with a data-driven method known as spline-backfitted kernel (SBK) estimation. In Section 2.3, we introduce the spatio-temporal model, and compare the model’s performance assuming either a separable or a nonsepa-

vable covariance structure to evaluate whether separability can be assumed. In Section 3, we apply the model to irradiance data from the La Ola photovoltaic plant in Lanai, HI. Finally, we provide discussion and conclusions in Section 4.

2. Modeling Irradiance

Let $Q_{s,t}$ represent an observable process, e.g., measured GHI, at time t and location s for $t = 1, 2, \dots, T$ and $s = 1, 2, \dots, S$. If there is no interaction in time and space, the covariance function of $Q_{s,t}$ can be written as a product of two functions where one function is dependent on time only, and the other on location alone. Such a covariance function is called “separable.” However, when interactions in space and time are present, the covariance function is “nonseparable;” i.e., it cannot be factored into two separate functions. Spatio-temporal models with separable covariance are much easier to implement. But in the presence of space-time interaction, separable models do not perform well, and can lead to misleading or incorrect conclusions.

For modeling $Q_{s,t}$, consider

$$Q_{s,t} = R_{s,t} + Z_{s,t}, \quad t = 1, \dots, T, \quad s = 1, \dots, S, \quad (1)$$

where, at time t and location s , $R_{s,t}$ represents the true irradiance signal and $Z_{s,t}$ is a noise process. Furthermore, decompose the noise process into a sum of three terms,

$$Z_{s,t} = X_{s,t} + Y_{s,t} + \varepsilon_{s,t}, \quad (2)$$

where $X_{s,t}$ is a time series process at location s , $Y_{s,t}$ is a spatial process at time t , and $\varepsilon_{s,t}$ is a multivariate error process with mean zero and $TS \times TS$ covariance matrix $\Sigma(s, t)$. If the process is separable, then the covariance matrix can be written as $\Sigma(s, t) = \Lambda(t) \otimes \Gamma(s)$, where $\Lambda(t)$ is a $T \times T$ temporal covariance matrix, $\Gamma(s)$ is an $S \times S$ spatial covariance matrix, and \otimes is the Kronecker product (Woolrich et al., 2004).

There are a variety of methods for fitting separable spatio-temporal models to space-time data. A review of space-time analysis methods and their computational counterparts can be found in Harvill (2010) or Cressie and Wikle (2011). We consider three approaches to fitting model (2). The first approach fits a spatial model at each time. Then spatial residuals are computed, and for each location a time series model is fitted to the spatial residuals at each location. The second approach models the time series at each

location, computes time residuals, and then fits a spatial model at each time to the residuals. Both of these approaches carry the assumption that the covariance structure is separable in space and time. The third approach removes the separability assumption, jointly modeling time and space using the spatio-temporal model introduced in Section 2.4.

2.1. Modeling the Time Series Component

For modeling time series data arising from a dynamic process, such as solar irradiance, nonlinear models often out-perform linear models (Tong, 1993). Although the class of nonlinear time series models is infinitely large, there are many popular parametric nonlinear models including the bilinear model (Subba Rao and Gabr, 1984), the exponential autoregressive model (Haggan and Ozaki, 1981), and a variety of threshold autoregressive models (Tong, 1983; van Dijk, 1999). When one of these parametric models is known to be appropriate for analyzing the time series, it should be used for analyzing the series. However in the analysis of solar irradiance, no specific class of parametric nonlinear model has been shown to be generally applicable, and therefore we pursue a semiparametric approach. In this section, we examine only the time component of the model. So to ease notation, for the remainder of this section, we consider the location fixed, and suppress the s subscript; that is $X_{s,t} = X_t$ for a fixed value of s .

A highly versatile semiparametric model is the functional coefficient autoregressive model of order p (FCAR(p)), first introduced by Chen and Tsay (1993). The FCAR(p) model has an additive autoregressive structure, but with coefficients that vary as a function of some variable, u say, which can be exogenous to the series X_t . In the pure time series context, u is a lagged value of the series, and we write $u_t = X_{t-d}$. In this paper, we restrict the FCAR(p) models to those with $u_t = X_{t-d}$, and so define the FCAR(p) model as

$$X_t = m_0(u_t) + \sum_{j=1}^p m_j(u_t)X_{t-j} + \omega_t, \quad t = p+1, \dots, T \quad (3)$$

where $u_t = X_{t-d}$, $d \leq p$, $m_j(\cdot)$, $j = 0, 1, 2, \dots, p$ are measurable functions of u , and $\{\omega_t\}$ is a sequence of independent and identically distributed (IID) random variables with mean zero and constant variance.

Reasonable use of the FCAR(p) model requires only that the model is additive, and places few restrictions on the functional coefficients. To illustrate the versatility of the FCAR(p) model, note that if $m_0(u_t) = 0$, and

$m_j(u_t) = \alpha_j$, $j = 1, 2, \dots, p$ are constants, then the FCAR(p) reduces to a linear autoregressive model of order p , $X_t = \alpha_1 X_{t-1} + \dots + \alpha_p X_{t-p} + \omega_t$. Another example is, for each $j = 1, \dots, p$, the coefficients are of the form $m_j(X_{t-d}) = \alpha_j + \beta_j \exp\{-\delta X_{t-d}^2\}$. Then the FCAR(p) model reduces to the exponential autoregressive model of Haggan and Ozaki (1981). Moreover, the FCAR(p) formulation allows for a mixture of models; for example, $m_1(X_{t-d}) = \alpha_1$ and $m_2(X_{t-d}) = \alpha_2 + \beta_2 \exp\{-\delta X_{t-d}^2\}$. Fan and Yao (2003) contains a review of methods for fitting the FCAR(p) model, and related inferential procedures. In the following section, we propose a more recent, improved method for fitting the FCAR(p) model.

2.2. Spline-Backfitting Kernel Estimation

With no presupposed form for the functional coefficients, we propose a data-driven method for finding pointwise estimates of the functions $m_j(u)$, $j = 0, 1, 2, \dots, p$. A number of methods are proposed in the statistics literature. Chen and Liu (2001) and Cai et al. (2000) propose a kernel regression approach to fitting the model. Harvill and Ray (2006) extend the procedure to the case when the series is a vector process. More recently, spline-backfitted kernel (SBK) estimation has been proposed as a means for fitting semiparametric models like the FCAR(p) model. SBK estimation is an adaptation of the backfitting algorithm of Hastie and Tibshirani (1990), and combines the computational speed of splines with the asymptotic properties of kernel smoothing.

The SBK method uses an under-smoothed centered standard spline procedure to pre-estimate the $m_j(u)$, $j = 0, 1, 2, \dots, p$. These pre-estimates, also called “oracle” estimates, are used to find psuedo-responses. Then the pseudo-responses are used to estimate the $m_j(u)$ through a kernel estimator; e.g., the Nadaraya-Watson estimator. The SBK method was first proposed by Wang and Yang (2007) for estimating nonlinear additive autoregressive models. Wang and Yang (2009) adapt the SBK method for IID data, Liu et al. (2011) adapt it to generalized additive models, and Ma and Yang (2011) to partially linear additive models. Liu and Yang (2010) propose the SBK method for additive coefficient models.

The ability to estimate $m_j(u)$, $j = 0, 1, 2, \dots, p$ relies on the good approximation properties of spline estimators. For any $j = 0, 1, 2, \dots, p$, assume $m_j(\cdot)$ is sufficiently smooth. Without loss of generality, u can be defined on the compact interval $[0, 1]$. Define the integer $N \approx T^{2/5} \log T$, and let $H = (N + 1)^{-1}$. Let $0 = \xi_0 < \xi_1 < \dots < \xi_N < \xi_{N+1} = 1$ denote a sequence of

equally spaced knots. There is a set of basis functions $b_0(u), b_1(u), \dots, b_{N+1}(u)$ and a set of constants $\tilde{\lambda}_{0,j}, \tilde{\lambda}_{1,j}, \dots, \tilde{\lambda}_{N+1,j}$ such that the spline estimator of the j -th coefficient is

$$m_j(u) \approx \tilde{m}_j(u) = \sum_{k=0}^{N+1} \tilde{\lambda}_{k,j} b_k(u). \quad (4)$$

For the basis functions, we choose the linear B -spline basis, defined by

$$b_k(u) = \left(1 - \frac{|u - \xi_k|}{H}\right)_+ = \begin{cases} (N+1)u - k + 1, & \xi_{k-1} \leq u < \xi_k, \\ k + 1 - (N+1)u, & \xi_k < u \leq \xi_{k+1}, \\ 0, & \text{otherwise.} \end{cases}$$

The coefficients $\tilde{\lambda}_{0,j}, \tilde{\lambda}_{1,j}, \dots, \tilde{\lambda}_{N+1,j}$ are estimated via least squares; that is, the $\tilde{\lambda}_{k,j}$, $k = 0, 1, \dots, N+1$, $j = 0, 1, 2, \dots, p$ are the values of $\lambda_{k,j}$ that minimize the sum of squares

$$\sum_{t=p+1}^T \left[X_t - \sum_{j=1}^p \left\{ \sum_{k=0}^{N+1} \lambda_{k,j} b_k(u) \right\} X_{t-j} \right]^2 \quad (5)$$

The spline-estimated functional coefficients are then used to compute “pseudo-responses.” Specifically, for each $j' = 0, 1, 2, \dots, p, j' \neq j$, the pseudo-responses are defined by

$$\hat{W}_{t,j'} = X_t - \sum_{j=1, j \neq j'}^p \tilde{m}_j(u) X_{t-j}, \quad t = p+1, p+2, \dots, T.$$

For each $j' = 0, 1, 2, \dots, p$, let $\tilde{\mathbf{W}}_{j'} = (\tilde{W}_{p+1,j'}, \dots, \tilde{W}_{T,j'})'$ represent the vector of pseudo-responses, and define the matrix

$$\mathbf{M} = \text{diag} \{ K_h(X_{p+1-d} - u), \dots, K_h(X_{T-d} - u) \},$$

where $K_h(\cdot) = h^{-1}K(\cdot/h)$, $K(\cdot)$ is a kernel function, and $h > 0$ is a bandwidth. Then the SBK estimator of $m_{j'}(u)$ is

$$\hat{m}_{j'}(u) = \begin{pmatrix} 1 \\ 0 \end{pmatrix} \left(\frac{1}{T} \mathbf{C}' \mathbf{M} \mathbf{C} \right)^{-1} \frac{1}{T} \mathbf{C}' \mathbf{M} \tilde{\mathbf{W}}_{j'}, \quad (6)$$

where

$$\mathbf{C}' = \begin{bmatrix} X_{p+1} & X_{p+2} & \cdots & X_T \\ X_{p+1}(X_{p+1-d} - u) & X_{p+2}(X_{p+2-d} - u) & \cdots & X_T(X_{T-d} - u) \end{bmatrix}$$

The idea behind SBK estimation is to under-smooth in the pre-estimates in order to reduce the bias. This under-smoothing leads to a larger variance which is reduced in the kernel estimation step. The use of splines for the pre-estimates is computationally fast while using kernel smoothing provides convenient asymptotic results (Liu and Yang, 2010).

To illustrate, consider a series of $T = 500$ observations from the exponential autoregressive model of order $p = 2$ (EXPAR(2)) given by

$$X_t = \left\{ 0.5 - 1.1e^{-50X_{t-1}^2} \right\} X_{t-1} + \left\{ 0.3 - 0.5e^{-50X_{t-1}^2} \right\} X_{t-2} + 0.2\omega_t, \quad (7)$$

where the ω_t are standard normal errors. A time plot of a mean-centered realization of length 500 of such a series is given in Figure 1.

Figure 1 about here.

Since X_{t-1} is the functional variable, and is one of the autoregressive lags, the model in (7) must be rewritten and treated as

$$X_t = m_0(X_{t-1}) + m_1(X_{t-1})X_{t-2} + 0.2\omega_t.$$

Consequently the functional coefficients of the autoregressive terms are

$$m_0(u_t) = 0.5u_t - 1.1u_t e^{-50u_t^2} \quad \text{and} \quad m_1(u_t) = 0.3 - 0.5e^{-50u_t^2},$$

where $u_t = X_{t-1}$.

To estimate the functional coefficients, begin by accounting for the variability in the response due to the term $m_0(u_t)$. Remove that variability, and use the pseudo-responses to estimate $m_1(u_t)$. Noting that the maximum lag is 2, we have

1. For $j = 0$ in equation (4), fit a spline to the mean-centered data. The result is an estimate $\tilde{m}_0(u_t)$ of $m_0(u_t)$. Note that the sum of squares in equation (5) has no second sum, since we are considering only a single value of $j, j = 0$; that is, equation (5) reduces to

$$\sum_{t=3}^T \left\{ X_t - \sum_{k=0}^{N+1} \lambda_{k,0} b_k(u_t) \right\}^2$$

2. Compute pseudo-responses $\hat{W}_{t,1}$, $t = 3, \dots, T$ using

$$W_{t,1} = X_t - \tilde{m}_0(u_t), \quad t = 3, 4, \dots, T.$$

These pseudo-responses are a proxy for the original realization, but with the effect of the $m_0(u_t)$ removed.

3. Fit a kernel regression to the pseudo-responses to get the SBK estimate $\hat{m}_1(u_t)$ of $m_1(u_t)$.

Repeat the procedure, reversing the roles of m_0 and m_1 . To get the coefficients $\lambda_{k,2}$, $k = 0, 1, \dots, N + 1$ for the spline, minimize the sums of squares

$$\sum_{t=3}^T \left[X_t - \left\{ \sum_{k=0}^{N+1} \lambda_{k,0} b_k(u_t) \right\} X_{t-2} \right]^2.$$

The pseudo-responses $W_{t,2}$, $t = 3, 4, \dots, T$ are computed via

$$W_{t,2} = X_t - \tilde{m}_1(u_2) X_{t-2}.$$

Figure 2 shows the estimation results of a simulated series from the exponential autoregressive model in equation (7) with IID standard normal ω_t and 500 samples. The dark curves of dots are the estimated functions, and the solid (thin) lines are the true functions. The dashed lines are the 95% pointwise confidence bands.

Figure 2 about here.

2.3. Spatial Modeling for Lattice Data

For a fixed time t , consider a lattice process Y_s , $s = 1, 2, \dots, S$. In this section, to ease notation, the time index t is suppressed. Let \mathcal{N}_s represent a neighborhood around location s . The simultaneous autoregressive (SAR) model is defined as

$$Y_s = \sum_{j' \in \mathcal{N}_s} \beta_{s,j'} Y_{j'} + \delta_s,$$

where $\beta_{s,j'}$ is a set of coefficients that induces the spatial autocorrelation between locations j' and s in \mathcal{N}_s , and δ_s are independent, zero-mean, constant variance errors. The SAR model was first introduced by Whittle (1954). The adjective ‘‘simultaneous’’ describes the S autoregressions that occur simultaneously at each data location in the formulation. To fit this model in Section 3, we will employ a two nearest neighbor structure to define \mathcal{N}_s . The model is fitted using maximum likelihood estimators which are obtained using the R package `spdep` (Bivand et al., 2013).

2.4. Spatio-temporal Modeling

We now introduce two spatio-temporal models both of the form in (1). The first model we consider uses the noise process defined in (2) and assumes a separable covariance structure for this process. The time series structure, $X_{s,t}$, is modeled as an FCAR model using the SBK method. Values of p and d in (3) are allowed to vary between locations, and the spatial structure, $Y_{s,t}$, is modeled separately using a SAR model at each time. By modeling the time and space components separately, we are implicitly assuming separability. If this assumption is appropriate, then the order in which the two models are fit (time-then-space, or space-then-time) should not matter.

The second spatio-temporal model does not assume separability. Combining the FCAR(p) model with a generalized version of the SAR model, we define the space-time functional coefficient simultaneous autoregressive (FCSAR) model as

$$Z_{s,t} = \sum_{w=1}^b \sum_{\ell \in \mathcal{N}_s} \beta_{s,\ell,w} Z_{\ell,t-w} + \sum_{k=1}^{p_s} m_{k,s}(Z_{s,t-d_s}) Z_{s,t-k} + \varepsilon_{s,t}, \quad (8)$$

where b is the spatial time order for the spatial component in the model, $\beta_{s,\ell,w}$ is the spatial autocorrelation between locations s and ℓ at a time lag of w , $Z_{s,t-d_s}$ is a delay variable, and $\varepsilon_{s,t}$ are IID with mean zero and constant variance σ_ε^2 . We allow the values of p_s and d_s to vary among locations. The FCSAR model is based on the space-time simultaneously specified autoregressive model of Woolrich et al. (2004).

3. Application and discussion

To illustrate the utility and compare the performance of the proposed models, we model GHI data at the 1.2 MV La Ola PV plant on the island of Lanai, Hawaii. We chose to model GHI rather than POA irradiance to illustrate a more general application of our method. The La Ola PV plant contains a grid of 12 single-axis tracked arrays arranged in three columns and four rows covering a total area of approximately 250m by 250m. At the time this work was undertaken, the La Ola data comprised the only available irradiance data set with concurrent measurements from a regular grid of sensors across the footprint of a single PV power plant. However, the La Ola data are POA irradiance rather than GHI. Sandia National Laboratories and SunPower Corporation designed an irradiance measurement system in part

to study the effects of the movement of cloud shadows across the PV arrays on the power output of the plant (Kuszamaul et al., 2010). Plane-of-array (POA) irradiance (in W/m^2) is measured at the midpoint of each tracking array using LiCor-200 pyranometers.

Before fitting the models it is necessary to remove the diurnal trend, a step which we found somewhat difficult. Clear sky models are available for removing trends from measured GHI data; a review of some of these models can be found in Reno et al. (2012). We set out to use clear sky models to remove the diurnal trend, which would present no great difficulty for measured GHI. We know of no equivalent “clear-sky” model for POA irradiance (although, if the tracking algorithm is known with sufficient precision, such a model could be assembled by applying a GHI-to-POA translation model, e.g., the DISC model of Maxwell (1987) to the output of a clear-sky model). We translated POA irradiance to GHI by assuming the isotropic sky model for the sky diffuse irradiance and using concurrent measurements of diffuse horizontal irradiance (DHI) and direct normal irradiance (DNI) from a nearby rotating shadowband radiometer (RSR) operated by the National Renewable Energy Laboratory. Because tracker rotations are not measured we estimated the angle of incidence on the modules using a generic algorithm for single-axis tracking (Lorenzo et al., 2011). Even with the use of measured DHI and DNI, the estimated GHI profiles were not well-matched with the output of available clear-sky models, and the clear sky models performed poorly in removing the trend. Consequently, we removed the diurnal trend in the estimated GHI by using a local polynomial kernel regression implemented in the `KernSmooth` package (Wand, 2012) in the R programming software.

We selected one year (i.e., January 1, 2010 to December 31, 2010) of POA irradiance measurements, which are recorded every second. We observed little to no variability from one irradiance measurement to the next at one second intervals and consequently reduced the data by time averaging. We investigated time-averages of lengths of 30 seconds, 1 minute, 5 minutes, and 10 minutes. Longer time averages (e.g., 15 and 20 minutes) were also considered but did not appear to be significantly different from the 10 minute averages. Much of our exploratory work was done using 10-minute averaged data to reduce computational burdens.

The top time plot in Figure 3 contains the 10-minute time averages of estimated GHI in solid black superimposed with the local polynomial kernel regression estimate in dashed red for March 10. The bottom time plot contains the residuals, hereafter referred to as “transformed irradiance,” ob-

tained after removing the diurnal trend by subtracting the kernel fit.

Figure 3 about here.

Having removed the diurnal trend, we next examined a large number of time plots of GHI to find days with different variability characteristics. For each day, the weather condition was classified visually as being in one of three categories: clear, partly cloudy, and overcast, by the variability and magnitude of GHI. Figure 4 shows the 10-minute time averaged irradiance and the transformed irradiance a clear day (October 21), a partly cloudy day (April 1), and an overcast day (August 3).

Figures 4(a) through 4(c) about here.

For 2010, in Lanai, HI, only six days could be classified as “clear” throughout the entire day. For partly cloudy and overcast conditions, we found many days. For both of these weather conditions, six days in 2010 were randomly selected.

For each selected day, we explored whether assuming space-time covariance separability in (1) would be justified. Using the separable models we fit the data in two ways: space-then-time and time-then-space. If the separability assumption is appropriate, then the two models are equivalent and should yield similar results. For the space-then-time approach, we first fit the SAR model to the 16 sensors for each time, t . We obtain the residuals from the fitted SAR model, and then apply the FCAR model to each sensor separately. For the time-then-space model, we first fit the FCAR model to the detrended irradiance for each of the 16 sensors, and then the residuals from the fitted FCAR model are fit with the SAR model at each time point. For each approach the root mean square errors (RMSEs) (over all sensor locations and times) for eighteen days with three different weather conditions are found in the first two columns of Table 1. For all days considered in this study, the RMSE for the model that fit space first is considerably smaller than when time was fit first. This is a strong indication that the assumption of separable covariance structures is not supported and that nonseparable models should be employed.

For a fixed time t , because PV cells are at fixed locations, the spatial structure can properly be considered a lattice. Consequently, for the nonseparable model we fit the FCSAR model in (8) for spatial time orders $b = 1, 2$. The last two columns in Table 1 contain values of RMSE for these two fits.

The FCSAR model with $b = 2$ has the smallest RMSE for all 18 days, indicating the best fit among the models considered. For cloudy and partly cloudy conditions RMSE decreases substantially from $b = 1$ to $b = 2$ indicating that a lagged model is needed for greater prediction accuracy.

Table 1 about here.

Figures 5 through 7 contain six plots, grouped in three pairs. Each figure displays one sensor location for one day: a clear day (October 21, Figure 5); a cloudy day (April 1, Figure 6); and a partly cloudy day (August 3, Figure 7). For any one pair of plots, the top graph contains the GHI data represented by a solid black line, and the modeled GHI represented by a red dashed line. The bottom graph contains the detrended GHI data (solid black line) and the detrended modeled GHI (red dashed line). For all three days, the set of two plots labeled (a) were fit using a separable time-then-space approach; the two sets of plots labeled (b) were fit using a separable space-then-time approach; and the plots labeled (c) were fit using the nonseparable FCSAR model with $b = 2$.

Figures 5 through 7 about here.

The collection of figures illustrates the nonseparable approach yields the best fit, regardless of the weather conditions, which is in agreement with minimum RMSE in Table 1. However, where RMSE is an aggregate measure of goodness-of-fit, the plots illustrate that at individual time points, the goodness-of-fit is uniformly better for the nonseparable model.

Forecasting the FCSAR model in time is largely dependent on using the SBK method for forecasting the FCAR term in (8). In Patrick et al. (2015), methodology is presented for forecasting a FCAR model using the SBK method. In this paper, we examine the performance of forecasting (8) in space for unobserved locations by using cross-validation. We simulated unobserved locations by omitting one or several sensors from our data set, and compared FSCAR model performance with a commonly used interpolation technique to judge the potential improvement offered by the FCSAR model.

Unobserved data are often estimated by interpolating between nearby sensors; one such technique is natural neighbor interpolation which comprises a weighted average with weights determined by a Voronoi partition (Sibson, 1981). A Voronoi partition divides the space that contains the sensors into

regions. Each sensor will have a corresponding region consisting of all points closer to that sensor than to any other. We constructed a Voronoi partition on the set of training sensors along with the location of the missing sensor. For cross-validation, we took the weighted average of the training sensors where the weights are determined by the size of the regions. This weighted average is used for the prediction for the missing sensors.

We fit the FCSAR model to the training set of sensors with $b = 2$ and using a two nearest neighbor structure for \mathcal{N}_s . For each missing sensor, we determined the two nearest neighbors and predicted the irradiance by using the estimated β 's for those neighbors.

For our set of 16 sensors, we calculated the predictions with $k = 1, 2, 3, 4$ missing sensor locations. For $k > 1$, we predicted for each missing location one at a time. We calculated the root mean prediction error (RMPE) as

$$RMPE_{\Omega_i} = \frac{1}{Tk} \sum_{s \in \Omega_i} \left(\sum_{t=1}^T (\tilde{Z}_{s,t} - Z_{s,t})^2 \right),$$

where Ω_i is the i th set of k missing sensors, $\tilde{Z}_{s,t}$ is the predicted irradiance for the s th sensor at time t , and $Z_{s,t}$ is the observed irradiance. The $RMPE_{\Omega_i}$ is calculated for all $K = \binom{16}{k}$ possible combinations of k missing sensors. The mean RMPE is calculated as

$$\overline{RMPE}_k = \frac{1}{K} \sum_{i=1}^K RMPE_{\Omega_i}.$$

To compare the FCSAR model to the interpolation method, we take the ratio

$$\frac{\overline{RMPE}_k \text{ for FCSAR}}{\overline{RMPE}_k \text{ for interpolation}}.$$

The ratios for all 18 days are plotted in Figure 8. Ratios less than one indicates that the FCSAR model performs better at predicting the missing sensors. All ratios are less than one except for two days both of which are clear days.

Figure 8 about here.

To examine the effect of different time averaging windows on the FSCAR model's performance we fit the model for a range of time averaging windows, from 10 minutes down to 30 seconds. For each day, we calculated the model's RMSE as well as the adjusted coefficient of determination R_a^2 . The adjusted coefficient of determination R_a^2 quantifies the level of agreement between the data and a fitted model taking into account the number of variables used in the model:

$$R_a^2 = 1 - \frac{SS_{\text{Fit}} / (TS - \nu_{\text{Fit}})}{SS_{\text{Total}} / (TS)},$$

where

$$SS_{\text{Fit}} = \sum_{s=1}^S \sum_{t=1}^T \left(\tilde{Z}_{s,t} - Z_{s,t} \right)^2,$$

$$SS_{\text{Total}} = \sum_{s=1}^S \sum_{t=1}^T \left(Z_{s,t} - \bar{Z} \right)^2,$$

$$\bar{Z} = \frac{1}{TS} \sum_{s=1}^S \sum_{t=1}^T Z_{s,t},$$

$\tilde{Z}_{s,t}$ is the predicted irradiance for the s th sensor at time t , $Z_{s,t}$ is the observed irradiance, and ν_{Fit} is the number of parameters used in the fit. Since we are using kernel regression to fit the time series, we must estimate the number of parameters associated with that regression. For the SBK estimate of the k th coefficient function in (8), the effective number of parameters is the trace of the smoother matrix

$$\begin{pmatrix} 1 \\ 0 \end{pmatrix} \left(\frac{1}{T} \mathbf{C}' \mathbf{M} \mathbf{C} \right)^{-1} \frac{1}{T} \mathbf{C}' \mathbf{M}$$

in (6) (see Hastie and Tibshirani, 1990; Cai and Tiwari, 2000). We calculate the total number of parameters as the sum of the parameters in the first double sum in (8) plus the sum of the effective number of parameters for the FCAR term. The values of R_a^2 and RMSE are shown in Table 2. We show the fits of three days for the different time averages in Figures 9-11.

Table 2 about here.

Table 2 shows that as the time averaging window decreases, RMSE increases and R_a^2 decreases, both indicating increasing disagreement between data and model. However, as the time averaging window decreases,

variance in time averaged data at any individual location increases substantially (Figures 9-11). As ramps in the data increase in both magnitude and frequency the largest residuals of the fitted model also increase. Similar patterns are evident in the spatially-averaged data. Figure 12 compares distributions for the spatially averaged detrended irradiance data and corresponding distributions residuals for the fitted FSCAR model for a partly cloudy day. As the averaging window decreases., outliers increase in both the data and the model residuals also increase, leading to the increasing RMSE and decreasing R_a^2 evident in Table 2. However, the FCSAR model continues to fit the bulk of the data equally well across all time averaging windows, as is demonstrated by the relatively constant boxes and whiskers across the different time averages. Thus, the FCSAR model follows time averaged data equally well for various averaging windows.

Figures 9 through 11 about here.

Figure 12 about here.

4. Conclusion

We have presented a novel nonseparable spatio-temporal model for GHI data. This approach, termed the FCSAR model, outperforms a natural neighbor interpolation when predicting GHI at unobserved locations over the footprint of a PV system. We compared the nonseparable FCSAR model with simpler, separable models, and find little support for models that assume a separable covariance structure. The FCSAR model integrates an FCAR form for the time series component of the model and a SAR form for the spatial component. The FCAR(p) form of the time series component of our nonseparable model makes the FCSAR model flexible and reliable, and may be suitable for fitting irradiance data in general. Currently, the model is fit separately on each day. Further research will consider validating the fitted models by comparing predicted aggregate irradiance with generated power for a much larger solar power plant than La Ola. Future work may also explore adding a weather condition covariate that will allow the model to be fit over days with different weather conditions, by permitting the coefficient functions in the time series structure to vary based on weather condition.

Acknowledgments

The research was performed under contract (PO 1303122) with Sandia National Laboratories, a multi-program laboratory managed and operated by Sandia Corporation, a wholly owned subsidiary of Lockheed Martin Corporation, for the U.S. Department of Energy's National Nuclear Security Administration under contract DE-AC04-94AL85000. Dr. Patrick's work was largely completed as a part of his dissertation work while he was at Baylor University. The authors thank Justin Sims for his help in creating the graphs provided in the figures throughout the manuscript.

References

- Bivand, R., with contributions by Micah Altman, Anselin, L., Assuno, R., Berke, O., Bernat, A., Blanchet, G., Blankmeyer, E., Carvalho, M., Christensen, B., Chun, Y., Dormann, C., Dray, S., Halbersma, R., Krainski, E., Legendre, P., Lewin-Koh, N., Li, H., Ma, J., Millo, G., Mueller, W., Ono, H., Peres-Neto, P., Piras, G., Reder, M., Tiefelsdorf, M., Yu., D., 2013. spdep: Spatial dependence: weighting schemes, statistics and models. R package version 0.5-56.
- Cai, Z., Fan, J., Yao, Q., 2000. Functional coefficient regression models for nonlinear time series. *Journal of the American Statistical Association* 95, 941–956.
- Cai, Z., Tiwari, R.C., 2000. Application of a local linear autoregressive model to bod time series. *Environmetrics* 11, 341–350.
- Chen, R., Liu, L., 2001. Functional coefficient autoregressive models: estimation and tests of hypotheses. *Journal of Time Series Analysis* 22, 151–173.
- Chen, R., Tsay, R., 1993. Functional coefficient autoregressive models. *Journal of the American Statistical Association* , 298–308.
- Cressie, N., Wikle, C., 2011. *Statistics for Spatio-Temporal Data*. John Wiley & Sons, Inc., Hoboken, New Jersey.
- van Dijk, D., 1999. *Smooth Transition Models: Extension and Outlier Robust Inference*. Ph.D. thesis. Erasmus University, Rötterdam, Netherlands.
- Fan, J., Yao, Q., 2003. *Nonlinear Time Series*. Springer, New York.
- Glasbey, C.A., 2001. Nonlinear autoregressive time series with multivariate gaussian mixtures as marginal distribution. *Journal of the Royal Statistical Society: Series C (Applied Statistics)* 50, 143–154.
- Glasbey, C.A., Allcroft, D.J., 2008. A spatiotemporal autoregressive moving average model for solar radiation. *Journal of the Royal Statistical Society: Series C (Applied Statistics)* 57, 343–355.

- Haggan, V., Ozaki, T., 1981. Modelling nonlinear random vibrations using an amplitude-dependent autoregressive time series model. *Biometrika* 68, 189–196.
- Harvill, J.L., 2010. Spatio-temporal processes, in: *Wiley Interdisciplinary Reviews: Computational Statistics*. John Wiley & Sons, Inc., New York. volume 2, pp. 375–382.
- Harvill, J.L., Ray, B.K., 2006. Functional coefficient autoregressive models for vector time series. *Computational Statistics and Data Analysis* 50, 3547–3566.
- Hastie, T.J., Tibshirani, R.J., 1990. *Generalized Additive Models*. volume 43. Chapman & Hall/CRC, Boca Raton.
- Kuszamaul, S., Ellis, A., Stein, J., Johnson, L., 2010. Lanai high-density irradiance sensor network for characterizing solar resource variability of mw-scale pv system, in: *35th Photovoltaic Specialists Conference*, Honolulu, HI.
- Liu, R., Yang, L., 2010. Spline-backfitted kernel smoothing of additive coefficient model. *Econometric Theory* 12, 29–59.
- Liu, R., Yang, L., Härdle, W.K., 2011. Oracally Efficient Two-Step Estimation of Generalized Additive Model. Technical Report. Humboldt University, Collaborative Research Center 649.
- Lorenzo, E., Narvarte, L., Munoz, J., 2011. Tracking and back-tracking. *Progress in Photovoltaics: Research and Applications* 19, 747–753.
- Ma, S., Yang, L., 2011. Spline-backfitted kernel smoothing of partially linear additive model. *Journal of Statistical Planning and Inference* 141, 204–219.
- Maxwell, E.L., 1987. A quasi-physical model for converting hourly global horizontal to direct normal insolation. Technical Report. Solar Energy Research Institute, Golden, CO.
- Paoli, C., Voyant, C., Muselli, M., Nivet, M.L., 2010. Forecasting of pre-processed daily solar radiation time series using neural networks. *Solar Energy* 84, 2146–2160.

- Patrick, J.D., Harvill, J.L., Sims, J.R., 2015. Spline-backfitted kernel forecasting for functional-coefficient autoregressive models. Submitted to Computational Statistics & Data Analysis. Manuscript available at <http://arxiv.org/abs/1502.03486>.
- Reikard, G., 2009. Predicting solar radiation at high resolutions: A comparison of time series forecasts. *Solar Energy* 83, 342–349.
- Reno, M.J., Hansen, C.W., Stein, J.S., 2012. Global Horizontal Irradiance Clear Sky Models: Implementation and Analysis. Technical Report SAND2012-2389. Sandia National Laboratories. Albuquerque, NM.
- Sibson, R., 1981. A brief description of natural neighbour interpolation. *Interpreting multivariate data* 21.
- Subba Rao, T., Gabr, M.M., 1984. An Introduction to Bispectral Analysis and Bilinear Time Series Models. Springer, Berlin.
- Tong, H., 1983. Threshold Models in Nonlinear Time Series Analysis. Lecture Notes in Statistics, Springer, New York.
- Tong, H., 1993. Non-linear Time Series: A Dynamical System Approach. Oxford Statistical Science Series, Oxford University Press, United Kingdom.
- Wand, M., 2012. KernSmooth: Functions for kernel smoothing for Wand & Jones (1995). R package version 2.23-8.
- Wang, J., Yang, L., 2009. Efficient and fast spline-backfitted kernel smoothing of additive models. *Annals of the Institute of Statistical Mathematics* 61, 663–690.
- Wang, L., Yang, L., 2007. Spline-backfitted kernel smoothing of nonlinear additive autoregression model. *Annals of Statistics* 35, 2474–2503.
- Whittle, P., 1954. On stationary processes in the plane. *Biometrika* 41, 434–449.
- Woolrich, M.W., Jenkinson, M., Brady, J.M., Smith, S.M., 2004. Fully bayesian spatio-temporal modeling of fmri data. *Medical Imaging, IEEE Transactions on* 23, 213–231.

Yang, D., Jirutitijaroen, P., Walsh, W.M., 2012. Hourly solar irradiance time series forecasting using cloud cover index. *Solar Energy* .

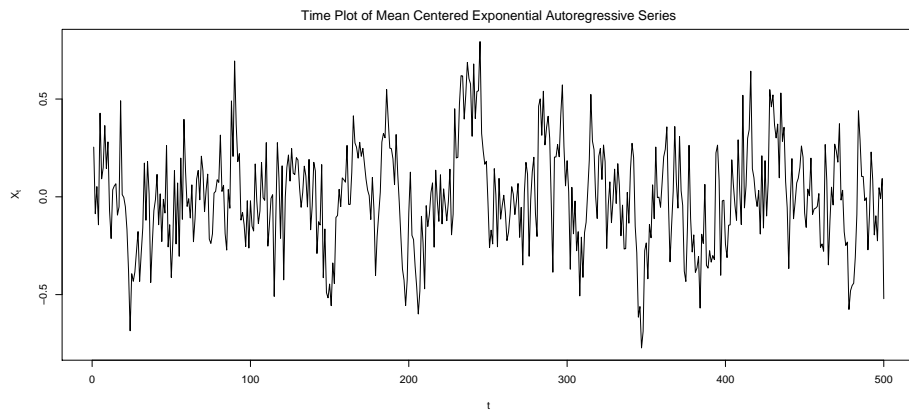


Figure 1: Mean-centered realization of length $T = 500$ from an EXPAR(2) model given in equation (7).

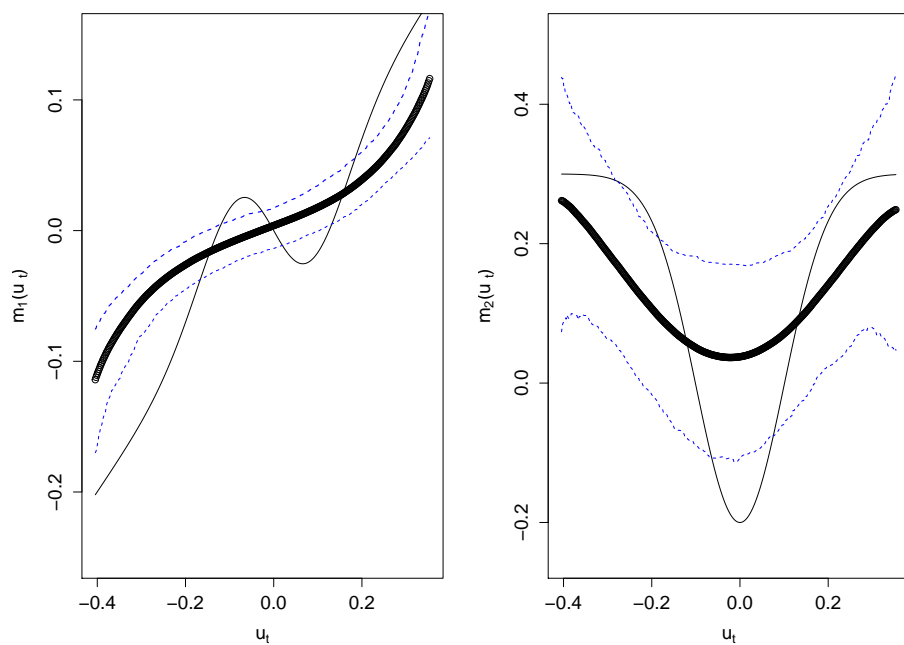


Figure 2: Spline-backfitted kernel estimates of the coefficients $m_0(u) = 0.5u - 1.1u \exp\{-50u^2\}$ (left panel) and $m_1(u) = 0.3 - 0.5 \exp\{-50u^2\}$ (right panel). Heavy curves are the estimates $\hat{m}_0(u)$ and $\hat{m}_1(u)$; thinner lines are the true functions $m_0(u)$ and $m_1(u)$; dashed lines are 95% confidence bands.

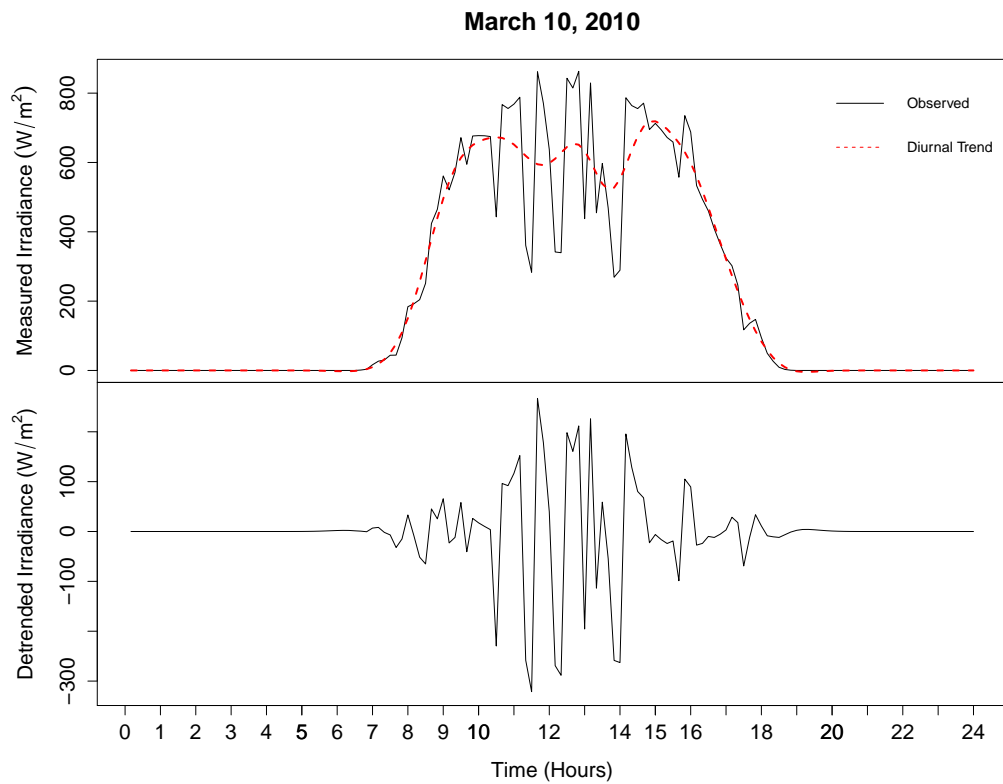
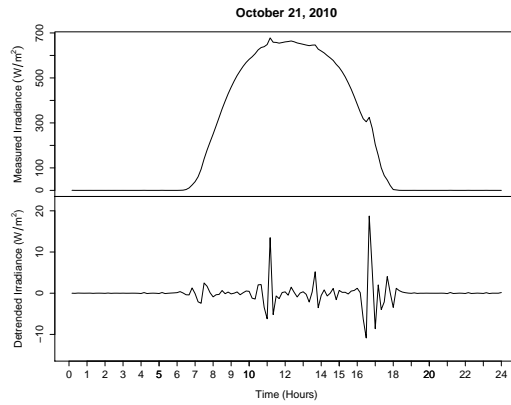
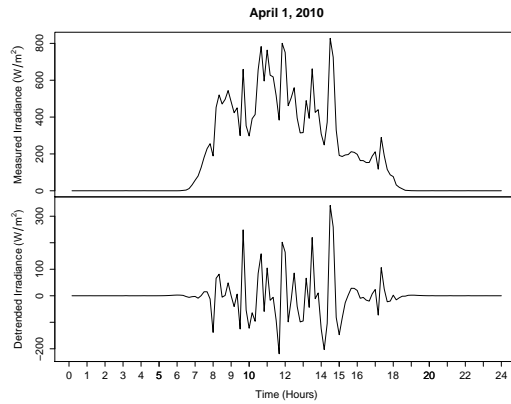


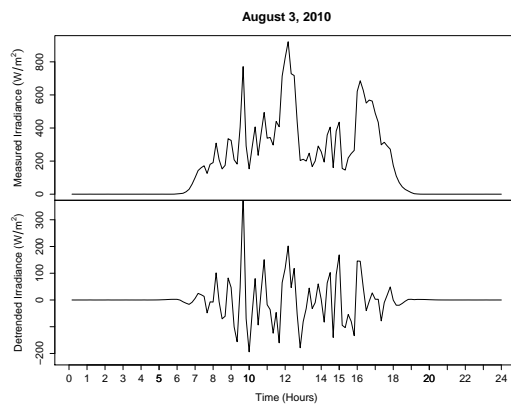
Figure 3: Top graph is the time plot of 10-minute averages (solid black) of irradiance measurements for March 10 with the local polynomial kernel estimate (dashed red) superimposed. The bottom plot is transformed irradiance (residuals after using local polynomial kernel regression to remove the diurnal trend).



(a) October 21, clear.



(b) April 1, partly cloudy.

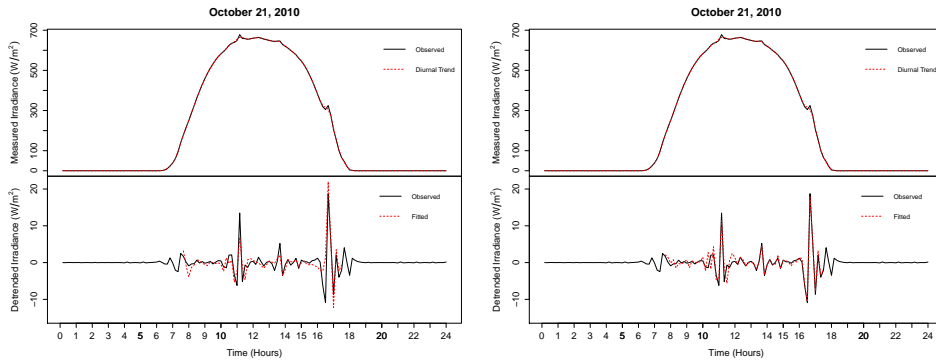


(c) August 3, overcast.

Figure 4: Time plots of 10-minute time averaged irradiance and of transformed irradiance for (a) a clear day, October 21, (b) a partly cloudy day, April 1, and (c) a overcast day, August 3.

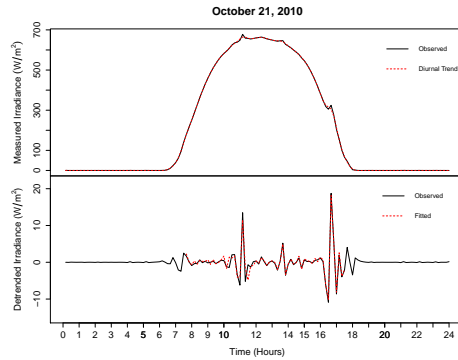
Table 1: Root mean squared error (RMSE) for the four spatio-temporal models of the days with clear, partly cloudy, and overcast conditions. Columns S-T and T-S contain the RMSE for the separable spatio-temporal models. Column S-T contains RMSE for data with the spatial component fit first, then time; Column T-S contains RMSE with the time component fit first, then space. The last two columns contain RMSE for the nonseparable FCSAR model with spatial time orders $b = 1$ and $b = 2$, respectively.

Condition	Date	Separable		FCSAR	
		S-T	T-S	$b = 1$	$b = 2$
Clear	Feb. 3	0.36	2.45	0.36	0.16
	Feb. 16	3.57	14.98	2.18	1.36
	Mar. 18	0.34	2.64	0.34	0.22
	Mar. 19	0.32	6.17	0.35	0.22
	Oct. 21	0.67	4.12	0.55	0.42
	Dec. 16	0.97	6.60	0.83	0.44
Partly Cloudy	Mar. 7	6.88	63.74	5.49	3.35
	Apr. 1	7.61	99.56	5.47	4.51
	May 10	5.91	56.86	4.90	3.72
	June 4	8.46	51.58	4.84	3.36
	June 28	3.63	55.10	2.39	1.76
	Nov. 15	10.39	58.24	7.14	6.00
Overcast	Feb. 1	7.52	62.61	6.20	4.88
	Mar. 15	12.82	118.23	9.12	5.50
	Apr. 6	5.66	48.15	2.97	2.43
	May 31	11.44	91.35	5.92	5.08
	Aug. 3	5.63	65.81	3.93	2.82
	Oct. 27	4.07	94.30	3.10	1.89



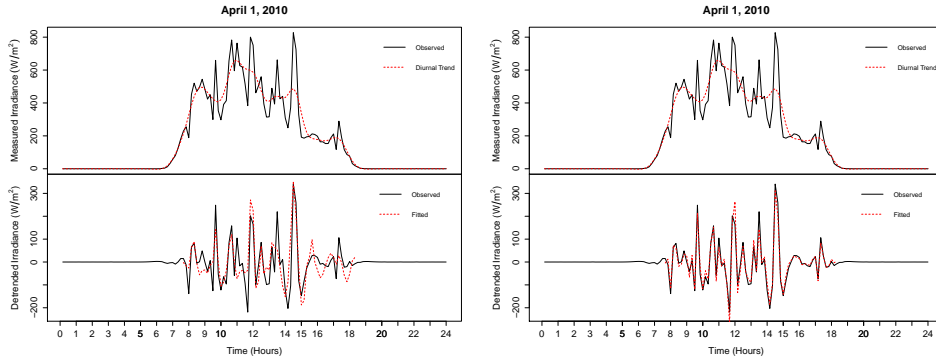
(a) October 21, Time-Space.

(b) October 21, Space-Time.



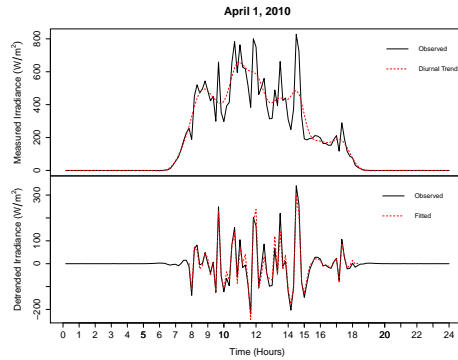
(c) October 21, Nonseparable.

Figure 5: Time plots of 10-minute time averaged irradiance and of transformed irradiance with predicted values superimposed in red for a clear day, October 21. Forecasting was conducted using the (a) time-then-space fitting (b) space-then-time fitting (c) nonseparable model.



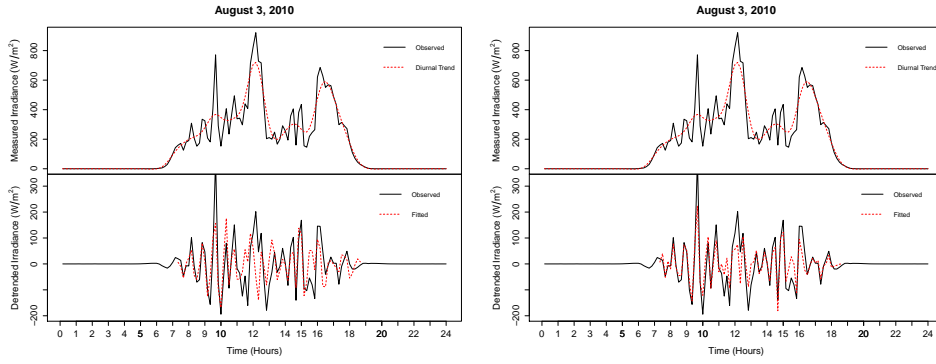
(a) April 1, Time-Space.

(b) April 1, Space-Time.



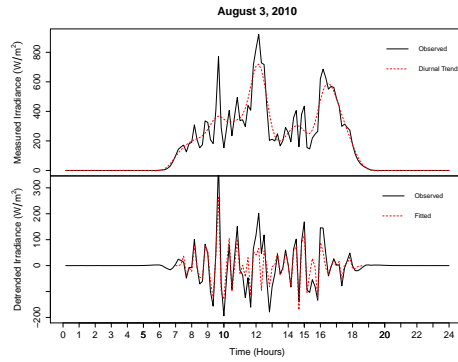
(c) April 1, Nonseparable.

Figure 6: Time plots of 10-minute time averaged irradiance and of transformed irradiance with predicted values superimposed in red for a partly cloudy day, April 1. Forecasting was conducted using the (a) time-then-space fitting (b) space-then-time fitting (c) nonseparable model.



(a) August 3, Time-Space.

(b) August 3, Space-Time.

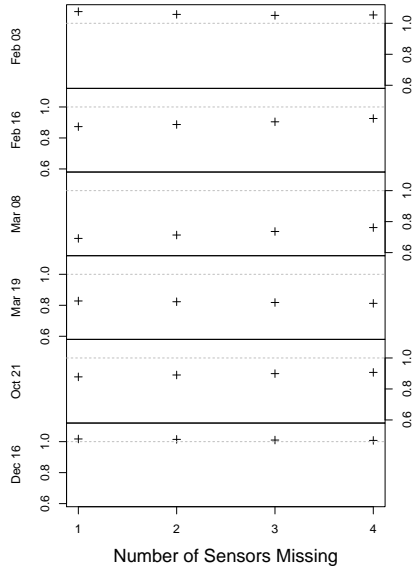


(c) August 3, Nonseparable.

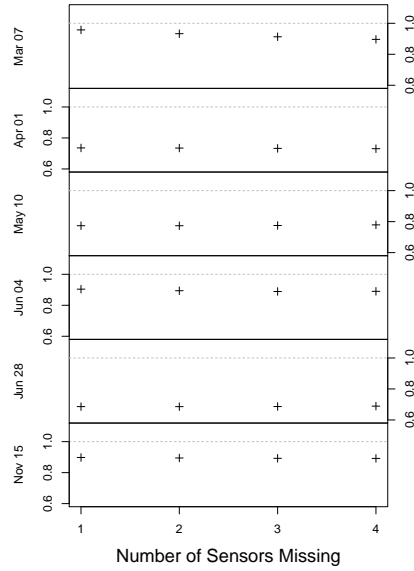
Figure 7: Time plots of 10-minute time averaged irradiance and of transformed irradiance with predicted values superimposed in red for an overcast day, August 3. Forecasting was conducted using the (a) time-then-space fitting (b) space-then-time fitting (c) nonseparable model.

Table 2: Root mean squared error (RMSE) for the nonseparable spatio-temporal models with $b = 2$ of the days with clear, partly cloudy, and overcast conditions. The columns are the RMSE for data at 30-second, 1-minute, 5-minute, and 10-minute averages. The values in parenthesis are the R_a^2 .

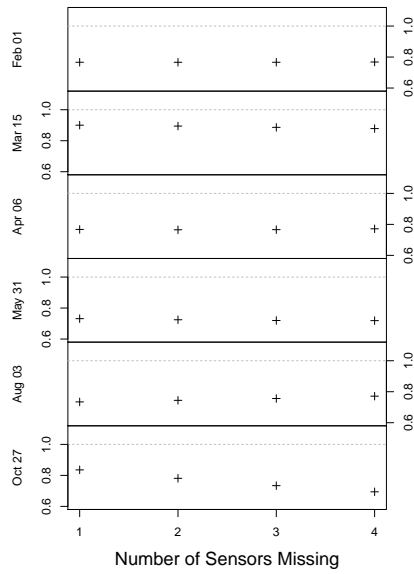
Condition	Date	30-sec	1-min	5-min	10-min
Clear	Feb. 3	0.38 (0.990)	0.30 (0.993)	0.19 (0.999)	0.16 (0.999)
	Feb. 16	4.98 (0.952)	3.68 (0.970)	1.82 (0.988)	1.36 (0.963)
	Mar. 18	1.79 (0.970)	0.99 (0.989)	0.42 (0.999)	0.22 (0.992)
	Mar. 19	0.81 (0.999)	0.63 (0.998)	0.32 (0.952)	0.22 (0.993)
	Oct. 21	3.94 (0.846)	2.21 (0.926)	0.67 (0.991)	0.42 (0.983)
	Dec. 16	0.67 (0.998)	0.61 (0.998)	0.49 (0.952)	0.44 (0.993)
Partly Cloudy	Mar. 7	25.66 (0.920)	17.68 (0.960)	5.42 (0.991)	3.35 (0.997)
	Apr. 1	31.75 (0.932)	24.65 (0.960)	6.99 (0.996)	4.51 (0.998)
	May 10	25.91 (0.927)	19.68 (0.954)	7.70 (0.987)	3.72 (0.999)
	June 4	22.05 (0.907)	20.60 (0.920)	7.21 (0.986)	3.36 (0.995)
	June 28	13.85 (0.935)	10.12 (0.966)	3.88 (0.994)	1.76 (0.999)
	Nov. 15	27.69 (0.908)	22.56 (0.935)	9.24 (0.979)	6.00 (0.987)
Overcast	Feb. 1	26.46 (0.899)	24.12 (0.917)	9.27 (0.982)	4.88 (0.993)
	Mar. 15	27.85 (0.938)	20.29 (0.968)	6.05 (0.996)	5.50 (0.997)
	Apr. 6	24.22 (0.883)	19.44 (0.930)	4.01 (0.997)	2.43 (0.997)
	May 31	42.26 (0.899)	30.26 (0.943)	9.60 (0.988)	5.08 (0.997)
	Aug. 3	25.92 (0.948)	20.59 (0.966)	6.15 (0.995)	2.82 (0.998)
	Oct. 27	7.20 (0.977)	5.52 (0.989)	2.61 (0.998)	1.89 (0.999)



(a) Clear days.

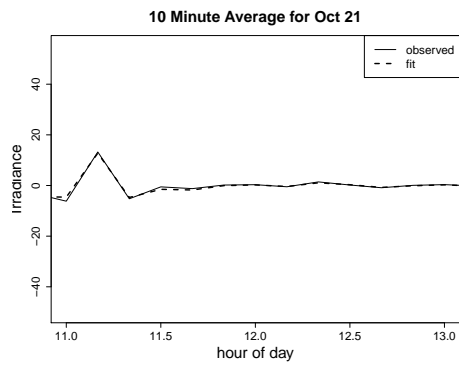


(b) Partly cloudy days.

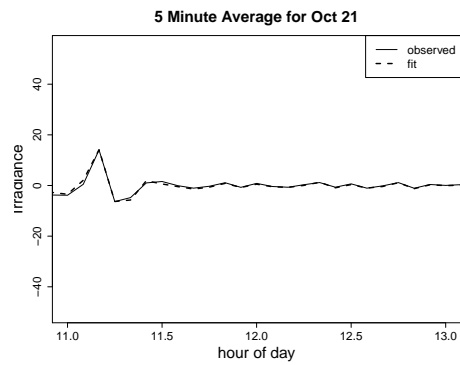


(c) Overcast days.

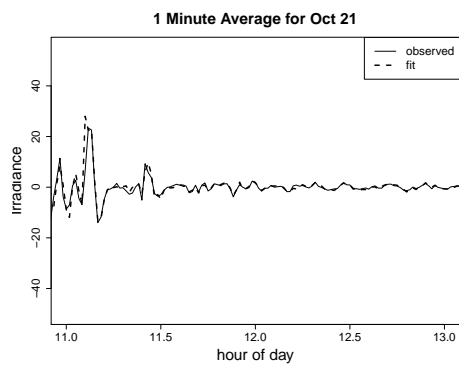
Figure 8: Plots of the ratios of the RMPE for (a) the clear days, (b) the partly cloudy days, and (c) the overcast days. The ratios are calculated as the RMPE of the FCSAR model divided by the RMPE of linear interpolation.



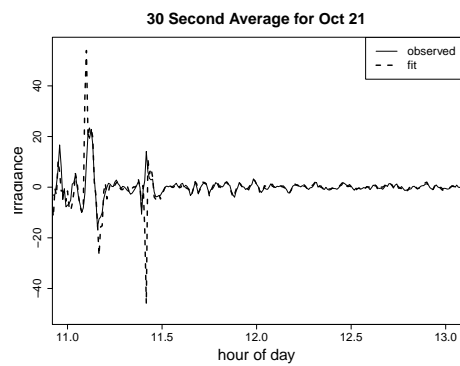
(a)



(b)



(c)



(d)

Figure 9: Plots of the detrended observed irradiance and the fit of the FCSAR model for sensor 1 from 11:00 to 13:00 on October 21 (a clear day). The different plots are for different averages: (a) 10 minutes, (b) 5 minute, (c) 1 minute, and (d) 30 second.

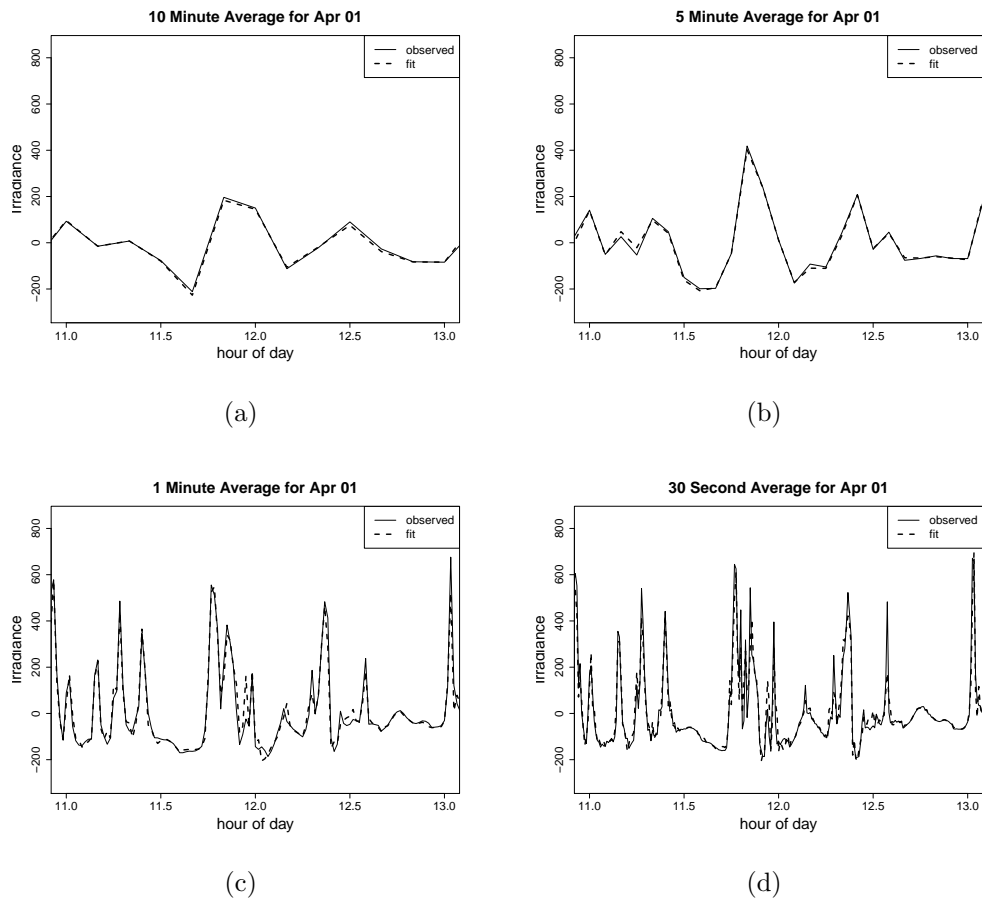
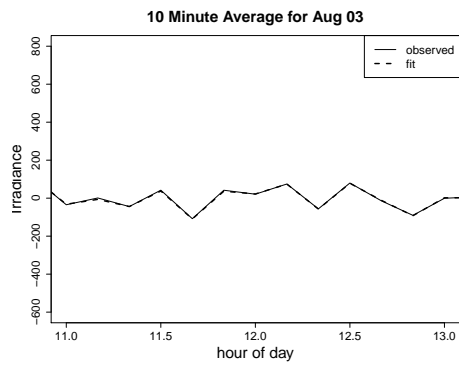
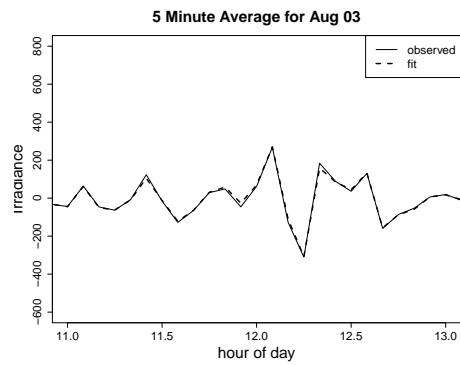


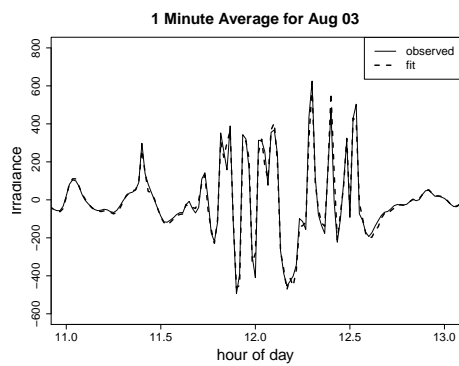
Figure 10: Plots of the detrended observed irradiance and the fit of the FCSAR model for sensor 1 from 11:00 to 13:00 on April 1 (a partly cloudy day). The different plots are for different averages: (a) 10 minutes, (b) 5 minute, (c) 1 minute, and (d) 30 second.



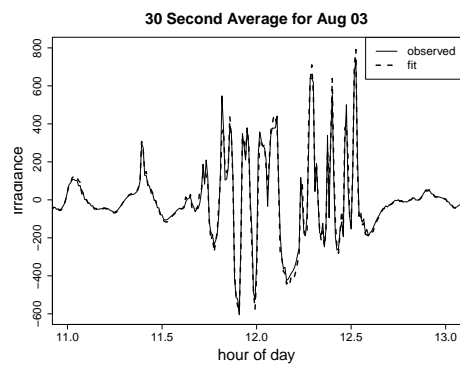
(a)



(b)

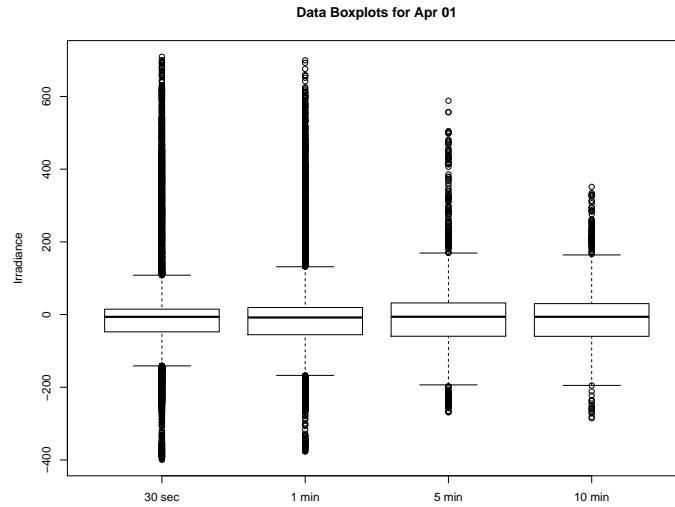


(c)

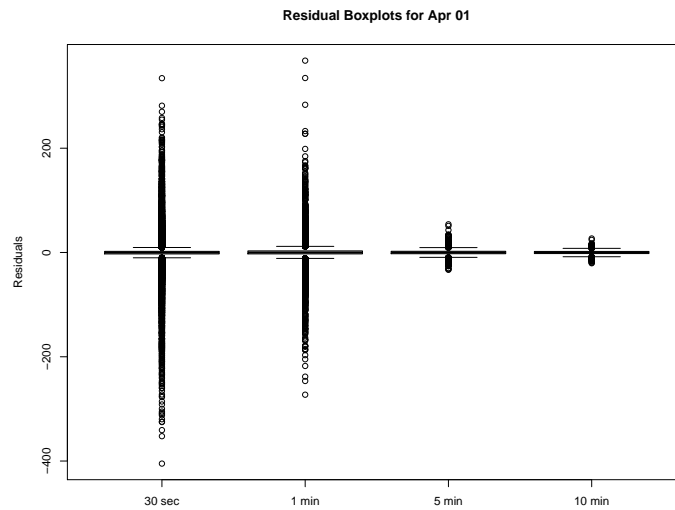


(d)

Figure 11: Plots of the detrended observed irradiance and the fit of the FCSAR model for sensor 1 from 11:00 to 13:00 on August 3 (an overcast day). The different plots are for different averages: (a) 10 minutes, (b) 5 minute, (c) 1 minute, and (d) 30 second.



(a)



(b)

Figure 12: Boxplots for (a) the observed detrended data and (b) the residuals of the fit of the FCSAR model with $b = 2$ for April 1 (a partly cloudy day).